PHYSICAL REVIEW B **94**, 054112 (2016)

Ferroelectric phase transitions in multiferroic $Ge_{1-x}Mn_xTe$ driven by local lattice distortions

Dominik Kriegner,[1,*] Jürgen Furthmüller,[2] Raimund Kirchschlager,[3] Jan Endres,[1] Lukas Horak,[1] Petr Cejpek,[1]
Helena Reichlova,[4] Xavier Marti,[4] Daniel Primetzhofer,[5] Andreas Ney,[3] Günther Bauer,[3] Friedhelm Bechstedt,[2]
Vaclav Holy,[1] and Gunther Springholz[3]
[1]*Department of Condensed Matter Physics, Charles University in Prague, Ke Karlovu 5, 121 16 Praha 2, Czech Republic*
[2]*Institut für Festkörpertheorie und -optik, Friedrich-Schiller-Universität, Max-Wien-Platz 1, 07743 Jena, Germany*
[3]*Institute of Semiconductor and Solid State Physics, Johannes Kepler University Linz, Altenbergerstr. 69, 4040 Linz, Austria*
[4]*Institute of Physics ASCR, v.v.i., Cukrovarnická 10, 162 53 Praha 6, Czech Republic*
[5]*Ion Physics Department, The Ångström Laboratory, Uppsala University, P.O. Box 534, SE-75121, Sweden*

(Received 13 October 2015; revised manuscript received 27 July 2016; published 19 August 2016)

The evolution of local ferroelectric lattice distortions in multiferroic $Ge_{1-x}Mn_xTe$ is studied by x-ray diffraction, x-ray absorption spectroscopy, and density functional theory. We show that the anion/cation displacements smoothly decrease with increasing Mn content, thereby reducing the ferroelectric transition from 700 to 100 K at $x = 0.5$, where the ferromagnetic Curie temperature reaches its maximum. First principles calculations explain this quenching by different local bond contributions of the Mn 3*d* shell compared to the Ge 4*s* shell in excellent quantitative agreement with the experiments.

DOI: 10.1103/PhysRevB.94.054112

I. INTRODUCTION

Multiferroics combining ferroelectric (FE) and ferromagnetic (FM) order in one and the same material [1,2] have triggered immense interest due to their unique properties that open promising avenues for device applications [3,4]. Materials combining ferroelectricity and ferromagnetism in a single phase are, however, very rare. In $Ge_{1-x}Mn_xTe$ these two properties coexist and couple to each other [5]. This is because ferroelectricity is induced by the huge lattice distortion of the GeTe host material, whereas ferromagnetism is caused by the local spins of the Mn ions that couple via the free carriers in the system. Due to high solubility of Mn in GeTe and the high hole concentration, FM transition temperatures up to 190 K have been achieved [5–9], which are amongst the highest of all ferromagnetic semiconductors [10].

While the ferromagnetic properties of $Ge_{1-x}Mn_xTe$ have been studied in detail [5–9,11–14], the influence of Mn doping on the ferroelectric properties [15,16] are not yet understood. Ferroelectricity is due to the inversion symmetry breaking caused by the displacement of the anion and cation sublattice relative to each other [17,18]. For GeTe, this displacement is as large as ~0.3 Å [17,18], which results in a high FE transition temperature of ~700 K [19,20] and was shown to be connected with a softening of elastic parameters [21]. The strong ferroelectricity leads to a giant Rashba splitting of the bands [22–24], making GeTe a prime member of ferroelectric Rashba semiconductors that provide additional features for spintronic devices [22]. For $Ge_{1-x}Mn_xTe$, however, the driving force for the electric phase transitions as well as the multiferroic coupling have not been fully identified. Analogously to GeTe, in $Ge_{1-x}Mn_xTe$ a ferroelectric phase transition caused by a relative displacement of the anion/cation sublattice occurs. These displacements and their relation to the multiferroic properties have yet been largely unexplored since direct measurements of electric polarization have been hampered by the high carrier concentration [25] needed for ferromagnetic interactions.

In this paper, we combine temperature dependent x-ray diffraction (XRD) and low temperature extended x-ray absorption fine structure spectroscopy (EXAFS) of high quality epitaxial $Ge_{1-x}Mn_xTe$ films to study the local lattice distortions of Ge and Mn atoms with respect to the surrounding Te atoms as a function of the alloy composition. This is complemented by *ab initio* density functional theory (DFT) calculations to derive the lowest energy configuration and evaluate the local bonding configurations. We reveal in experiments and DFT that Mn atoms are shifted significantly less than the Ge atoms and that the atomic shifts are gradually quenched with increasing Mn content. As a result, the energy difference between the ferroelectric (distorted) and paraelectric (cubic) phase monotonically decreases, in perfect agreement with the decrease in FE transition temperature. Since Mn is the key ingredient for magnetism, we conjecture that the magnetic ordering is affected too as the Mn-Te-Mn bonds bridging the superexchange magnetic interactions start changing right at the onset of the ferroelectric transition.

The paper is organized as follows. In Sec. II, we describe the sample fabrication, the temperature dependent XRD experiments, as well as EXAFS measurements. In Sec. III we present first principle calculations of the GeMnTe structure, and in Sec. IV we discuss our results.

II. EXPERIMENTS

A. GeMnTe thin film growth and characterization

For our studies epitaxial $Ge_{1-x}Mn_xTe$ films with x_{Mn} ranging from 0 to 0.48 and thickness of 500 nm were grown by molecular beam epitaxy (MBE) onto $BaF_2(111)$ substrates at 280 °C using GeTe, Mn, and Te as beam flux sources [8,9]. The chemical composition was controlled by the Mn/GeTe flux ratio and 2D growth was sustained in all cases by fine tuning of the growth conditions [9]. A protective Al_2O_3 cap of 20 nm thickness was deposited *ex situ*

---

[*] kriegner@mag.mff.cuni.cz

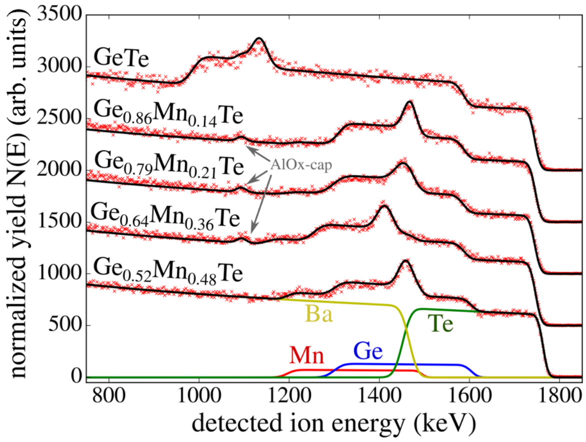

FIG. 1. Rutherford backscattering spectra for a series of $Ge_{1-x}Mn_xTe$ films with different Mn content. Shown are the experimental normalized yield $N(E)$ (red symbols) and the respective simulation (black line). For the sample with 48% Mn also the contributions of the individual elements are included. In addition to the elements in the film (Ge,Mn,Te) and substrate (Ba) also a signal from the protective Al_2O_3 cap was observed. Curves are shifted vertically for clarity.

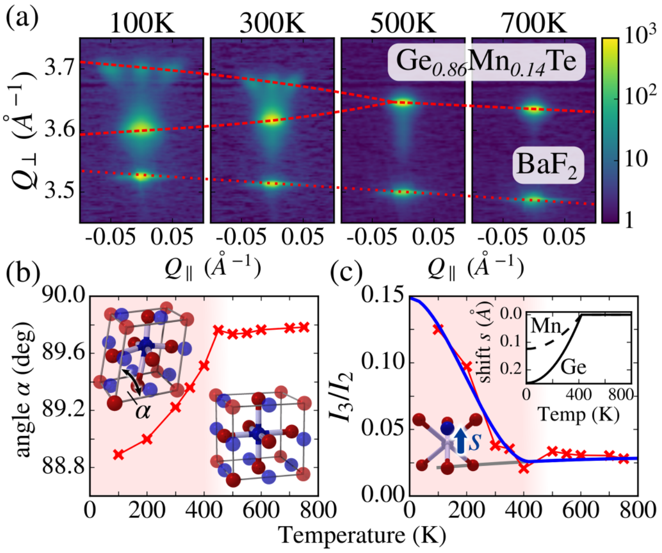

FIG. 2. (a) Temperature dependent (222) XRD reciprocal space maps of $Ge_{0.86}Mn_{0.14}Te$ on $BaF_2(111)$. Dashed/dotted lines indicate the change of the peak position and their splitting due to the paraelectric/ferroelectric phase transition at 420 K. (b) Measured unit cell angle and (c) intensity ratio I_3/I_2 between the (333) and (222) Bragg peaks versus temperature. The blue and gray lines are model calculations including and excluding the effect of the anion-cation displacement s as shown by the inset. The unit cells above and below the FE phase transition are shown in (b).

after growth. Rutherford backscattering spectrometry (RBS) was employed to quantify the chemical composition of the thin films from comparison with well-known scattering cross sections of the elements [26]. $^4He^+$ ions with a primary energy of 2 MeV were directed on the samples and detected in a Si detector situated at a scattering angle of 170 degrees. To avoid any influence from ion channeling, caused by the single crystallinity of the samples, their angular orientation was modified by small arbitrary steps around an equilibrium position in each measurement [27]. The evaluation of the RBS spectra was performed using the simulation code SIMNRA [28] to obtain film thicknesses and concentration profiles. Figure 1 shows the spectra and corresponding simulations for a series of samples with different Mn content. The main source for uncertainties in the deduced concentrations stems from counting statistics. We note that the relative signals of Ge and Te allow for a cross check of the deduced Mn concentrations resulting in a total uncertainty of ±4% in the Mn concentrations. Apart from the information on the chemical composition of the GeMnTe films, the RBS spectra also confirm the homogeneous distribution of Mn across the film depth, i.e., there is no indication for the occurrence of Mn segregation within the resolution limits of this method.

In order to confirm the structural homogeneity we also performed XRD investigations as shown in the Supplemental Material Fig. S1 (Ref. [29]). All epilayers up to $x_{\mathrm{Mn}} = 0.48$ solely exhibit the cubic rock salt or rhombohedral structure and do not show any signs of secondary NiAs-type or zinc blende MnTe phases [9]. These additional phases are only observed when the Mn concentration is increased beyond the solubility limit $x_{\mathrm{Mn}} > 0.5$ (Fig. S1 in Ref. [29]) for which reason such samples were excluded from further investigations. The magnetic properties were evaluated using a superconducting quantum interference device (SQUID), showing that all layers are ferromagnetic with FM Curie temperatures T_C^{FM} rising with Mn content as shown in the supplemental Fig. S2 in Ref. [29]. From the saturation magnetization at low temperatures we have calculated a magnetic moment of 1.66, 1.61, and 1.14 μ_B/Mn for samples with $x_{\mathrm{Mn}} = 0.18, 0.24,$ and 0.44, respectively. This relatively low moment per Mn indicates magnetic compensation due to antiferromagnetic coupling of neighboring Mn atoms which naturally increases with increasing Mn content. This is consistent with the fact that MnTe itelf is an antiferromagnet [30] and also explains the decrease of the magnetic moment per Mn atom upon increase of the Mn composition. In particular we also note that no signs of a phase with high T_C^{FM} were found for samples with $x_{\mathrm{Mn}} < 0.2$, which authors in Ref. [14] assigned to inhomogeneous distributions of Mn. The p-type carrier concentration of the films was derived by Hall effect measurements and found to be consistently around 1–2 × 10^{21} cm^{-3} for x_{Mn} in the 10 to 48% range as shown in Fig. S3 in Ref. [29].

B. Temperature dependent x-ray diffraction

To characterize the ferroelectric phase transition, temperature dependent XRD experiments were performed from 80 to 750 K at beamline BM25 at the European Synchrotron Radiation Facility using 20 keV photons. 3D reciprocal space maps were recorded both at symmetric and asymmetric Bragg reflections. Figure 2(a) shows the 2D projections of the (222) maps [31] for $x_{\mathrm{Mn}} = 0.14$ as a function of temperature. Below 500 K, the $Fm\bar{3}m$ space group symmetry of the cubic rock salt phase is broken and the GeMnTe peak splits up into four peaks due to the ferroelectric phase transitions in which a multidomain rhombohedral R3m structure is formed with distortions along one of the four ⟨111⟩ body diagonal directions. The peak splitting rapidly increases with decreasing temperature, indicating an increase of the FE lattice distortion, i.e., decrease in the unit cell angle α below the critical phase temperature T_C^{FE} of 420 K as shown in Fig. 2(b). Equivalent reciprocal space maps for other samples with $x_{\mathrm{Mn}} = 0$ to 0.36 are shown in Fig. S4 in Ref. [29]. It is noted that in our epitaxial films with low Mn composition the domains with ferroelectric polarization in different ⟨111⟩ polarization axes are not equally populated but those with polarization perpendicular to the (111) surface are strongly favored, accounting for 90% of the film volume. With increasing Mn content the change of the strain and thermal expansion properties of the film leads to a stronger population of the domains with tilted ⟨111⟩ directions and correspondingly a strengthening of their Bragg peaks is observed in Fig. S4 in Ref. [29].

While the peak splitting and change of peak positions provide information on the unit cell angle α [Fig. 2(b)] and lattice parameter (see Fig. S5 in Ref. [29]), they are no proof for the existence of an anion/cation displacement as required for a FE phase transition. However, as shown by Fig. 2(c), at the onset of the lattice distortion also the diffracted intensities abruptly change, signifying a change in the internal unit cell structure at the structural transition. Note that with the Bragg peak intensity we probe the average structure only and cannot distinguish the type of transitions [32,33]. The I_3/I_2 intensity ratio between the (333) and (222) Bragg peaks [cf. Fig. 2(c)] is particularly sensitive to the sublattice displacements as without such a displacement, the intensity ratio would be practically constant over the whole temperature range [gray line in Fig. 2(c)]. Using the atomic displacement derived by EXAFS (see next subsection) and assuming a temperature dependence scaled to that of GeTe [17], we can perfectly describe the variation of the I_3/I_2 ratio without any further fitting parameter. The according calculation is described in detail in the Appendix.

Figure 3 further details the variation of the unit cell angle and intensity ratio as a function of temperature and Mn content. At low Mn concentration both parameters evidence the existence of a FE phase with rhombohedral lattice distortion and anion/cation sublattice shift from which the FE transition temperature is derived. At higher $x_{\mathrm{Mn}} \gtrsim 0.3$, we do not find an abrupt change in unit cell angle and intensity ratio down to 10 K (Fig. S5 in Ref. [29]), meaning that it becomes inherently difficult to detect the phase transition due to the fact that at high x_{Mn} the FE lattice distortions become very small. Nevertheless, a switching behavior of the spontaneous electric dipole moment, monitored by changes in the magnetocrystalline anisotropy, i.e., multiferroic behavior has been observed for $x_{\mathrm{Mn}} = 0.5$ up to temperatures of 100 K, while the ferromagnetic transition is at $T_C^{\mathrm{FM}} = 190$ K [5]. In agreement with our EXAFS data below, which at low temperature suggest a ferroelectric polarization even beyond the solubility limit, we can assume that also samples between $x = 0.2$ and 0.5 are ferroelectric. With our data and those reported in literature the multiferroic phase diagram of $\mathrm{Ge}_{1-x}\mathrm{Mn}_x\mathrm{Te}$ is obtained as presented in Fig. 3(c), displaying the FM and FE regions as a function of temperature and composition for thin films as well as bulk material. For the FM transition, T_C^{FM} values up to ∼190 K are obtained for $x_{\mathrm{Mn}} \sim 0.5$ [5,9] in good agreement with recent theoretical calculations of Fukushima *et al.* [11]. The scatter in the data is due to the strong dependence of T_C^{FM} on the growth conditions and carrier concentrations [9]. Ferroelectricity, on the other hand, pertains over the whole range of compositions with T_C^{FE} well above room temperature for $x_{\mathrm{Mn}} < 0.2$. For higher x_{Mn} the ferroelectric phase boundary indicated in Fig. 3(c) is approximated by interpolation between the $x_{\mathrm{Mn}} = 0.21$ and 0.5 values. Thus a very wide region of coexistence of FE and FM order is obtained.

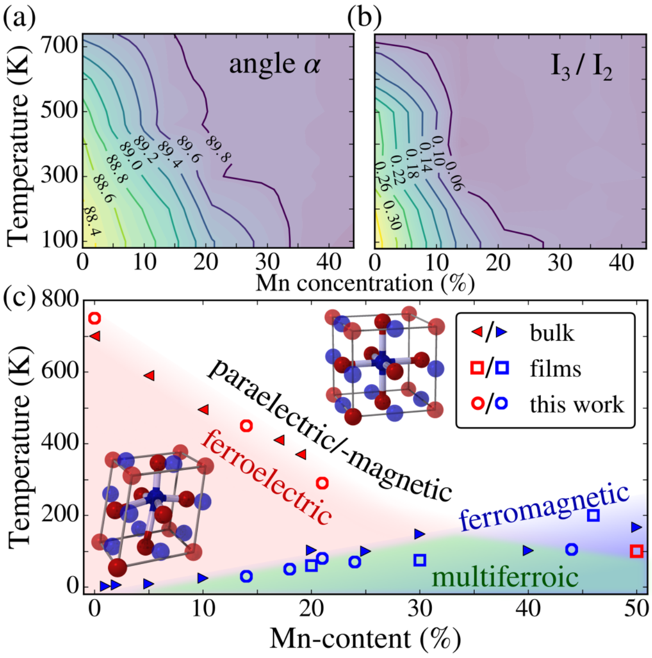

FIG. 3. (a),(b) Contour plots of the unit cell angle α and the I_3/I_2 intensity ratio of the (333) and (222) Bragg peaks that is strongly increased by the anion/cation sublattice displacements. (c) Multiferroic phase diagram of $\mathrm{Ge}_{1-x}\mathrm{Mn}_x\mathrm{Te}$ compiled from bulk [6,50] and thin-film [5,9] data. The blue data points show the FM and the red point the FE phase transition, and the open and closed symbols represent the data from films and bulk, respectively. The ferroelectricity spans over T_C^{FE} from above 700 K to 100 K for x_{Mn} increasing from 0 to 0.5, respectively, and ferromagnetism up to $T_C^{\mathrm{FM}} \sim 200$ K at $x_{\mathrm{Mn}} = 0.5$. The multiferroic regime where FE and FM coexist is indicated by the green region.

C. Extended x-ray absorption fine structure measurements

For quantitative derivation of the local anion/cation sublattice shifts and the origin of the ferroelectric polarization, EXAFS investigations were performed at the XAS beamline at Synchrotron Light Source ANKA. Fluorescence mode and grazing incidence geometry with polarization of the x-ray photons nearly perpendicular to the surface was used to enhance the sensitivity to the sublattice shifts. To distinguish between the shift of Ge and Mn atoms, measurements were performed at the Ge-K as well as Mn-K edges, respectively. Glitches due to the single crystalline nature of the films and substrate were suppressed by fine tuning of the incidence angle. The EXAFS oscillations in k space extracted from measurements at the Mn-K and Ge-K edges are shown in Fig. 4. The data

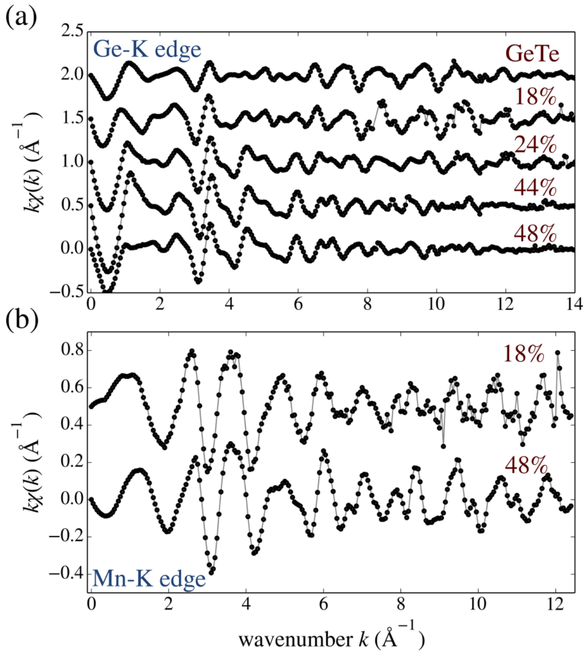

FIG. 4. Extended x-ray absorption fine structure k-space data extracted from our measurements at the Ge-K edge (a) and Mn-K edge (b). Shown is the oscillatory part of the fluorescence data after the sudden change of the fluorescence at the absorption edge was removed. The Mn content is indicated for every curve. The curves are vertically shifted for clarity.

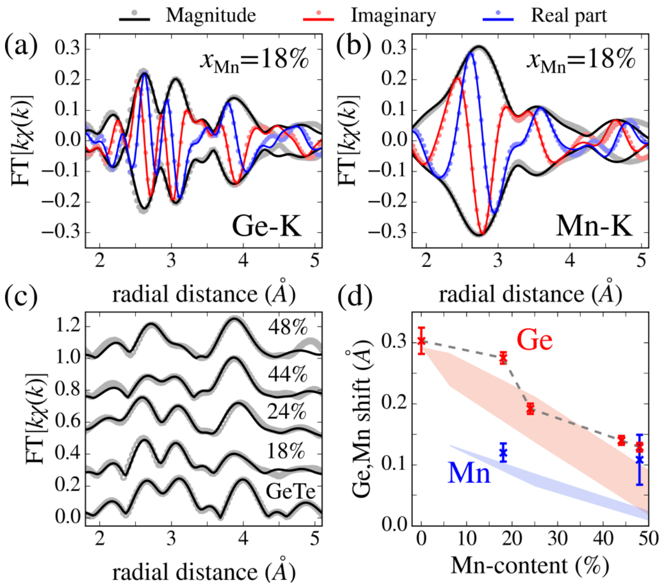

FIG. 5. EXAFS measurements of $Ge_{1-x}Mn_xTe$ at 15 K. r-space FT[$k\chi(k)$] data obtained at the Ge-K (a) and Mn-K (b) edge for $x_{\mathrm{Mn}} = 0.18$ show the real and imaginary part, as well as the magnitude of the experimental data (circles) together with fits (solid lines). (c) EXAFS data (circles) and fits (solid lines) for $Ge_{1-x}Mn_xTe$ as a function of compositions. (d) Derived off-center shift of Ge (red) and Mn (blue) atoms with respect to the surrounding Te atoms plotted as function of Mn content. The shaded areas indicates the DFT results from Fig. 6(c).

analysis was performed with the program Artemis [34]. Both absorption edges were fitted simultaneously and instead of independently fitting the different coordination shell radii we used the Mkfit-script [35] to directly fit the unit cell parameters (angle, lattice parameter, and shift of the atomic positions).

Detailed results for the sample with $x_{\mathrm{Mn}} = 0.18$ are presented in Figs. 5(a) and 5(b), where the Fourier transform (FT) of the $\chi(k)$ EXAFS data are shown with the respective fits. Figure 5(c) shows the magnitude of FT[$k\chi(k)$] for the whole investigated sample series obtained at the Ge-K edge. The displacement of Ge from the center of the surrounding six Te atoms leads to a splitting of the first coordination shell, manifested by double peaks in the r-space data at 2.7 and 3.1 Å in Fig. 5(a). Such large splitting is not observed at the Mn edge [Fig. 5(b)]. This is taken as a first hint that the shift of the Mn atoms is smaller. However, since the splitting also depends on the measurement conditions, further analysis of the EXAFS data was performed using the Artemis software to quantitatively derive the atomic shifts of the Ge and Mn sublattices. For the modeling of the EXAFS data of the ternary rhombohedrally distorted $Ge_{1-x}Mn_xTe$ alloy taken at the Ge and Mn edges we restrict ourselves to a system with a rigid Te sublattice and allow two separate shifts for the Mn and Ge atoms along the [111] direction. The justification for this simplification is the outcome of our first principles calculations (see below) which show that this is indeed the predominant change to reach the actual equilibrium atomic positions. A more sophisticated modeling of the EXAFS data of random alloys as previously done for ternary zinc-blende alloys like $Ga_{1-x}In_xAs$ or $Cd_{1-x}Mn_xTe$ in which also next nearest neighbors were considered [36,37] goes beyond the scope of the current study. Using such a model we indeed find that the off-center shift of the Mn atoms for $x_{\mathrm{Mn}} = 0.18$ is 0.12 Å and therefore 2.3 times smaller than that of the Ge atoms (0.27 Å), which is still close to the initial GeTe value. Such unusual large differences in the local displacements of the constituent elements have also been observed in ferroelectric lead zirconate titanate solutions ($PbZr_{1-x}Ti_xO_3$, $x \sim 0.5$), where the Zr atoms are found to be less shifted than the Ti atoms. In this case, however, the smaller Zr displacement does not hinder but strengthen the ferroelectricity in this system [38,39]. On the contrary, for $Ge_{1-x}Mn_xTe$ as shown by Fig. 5(d) both the Ge as well as Mn displacements decrease with increasing Mn content, i.e., FE is weakened upon Mn incorporation.

III. FIRST PRINCIPLES CALCULATIONS

To shed light on the local displacements and ground-state configuration of the atoms, first principles DFT calculations were performed using the Vienna *ab initio* simulation package (VASP) [40]. Pseudopotentials were generated within the projector-augmented wave (PAW) method [41] and an exchange-correlation functional including van der Waals (vdW) interactions according to Refs. [42] and [43] is used. Explicitly, we use the "optB86b-vdW" functional as implemented in VASP by Klimeš *et al.* which has proven excellent accuracy [44]. For the treatment of Mn we use in addition a DFT+U [45] correction for the Mn 3d states according to Dudarev *et al.* [46] with a U parameter of

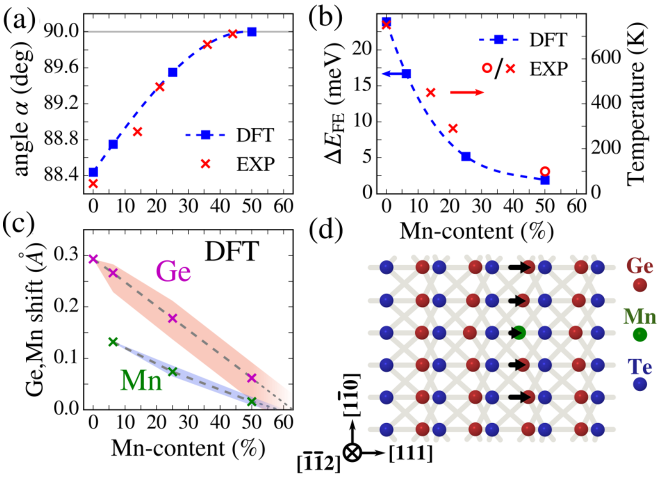

FIG. 6. Results of total energy minimizations in the DFT framework and their comparison with XRD and EXAFS data. (a) Rhombohedral unit cell angle α of $Ge_{1-x}Mn_xTe$ versus x_{Mn} at low temperatures. (b) Energy difference per atom pair between the cubic and rhombohedral structure of DFT compared with the experimental FE phased transition temperature. The experimental data points are from our work (crosses) and from Ref. [5] (open circle). Note the different vertical axes. (c) Calculated average off-center shifts of the Ge and Mn atoms (crosses) in dependence of the Mn content. The shaded areas represent the variation of the off-center displacements for different local atomic configurations as illustrated in (d). Dashed lines in (a)–(c) are guides to the eye and the dotted lines in (c) show the extrapolation of the atomic shifts beyond $x_{Mn} = 0.5$.

$U = 5$ eV [47]. We use ferromagnetically ordered magnetic moments found to be the stablest configuration in our experiments and previous DFT calculations [11] that identified the free carriers induced by Ge vacancies as a driving force for ferromagnetic ordering. A supercell of 64 atoms was populated by a random solid solution of (Ge,Mn)Te with compositions $x_{Mn} = 0, 0.0625, 0.25, 0.5$ in the rock-salt configuration. The actual equilibrium atomic positions and unit cell shape were obtained by total energy minimization without imposing any symmetry restrictions.

For all compositions the rhombohedral structure is found to be lower in energy compared to the cubic phase and the calculated lattice deformations perfectly reproduce the experimental data as demonstrated by Fig. 6(a). Thus, at low temperatures the ferroelectric phase prevails. The numerically optimized lattice parameters continuously decrease from 6.02 Å to 5.96 Å for $x_{Mn} = 0$ to 0.5 and therefore also describe the experimental trends shown in Fig. S5 in Ref. [29], however, with a slight trend to overestimate the lattice spacing. The energy difference per atom pair between the cubic and rhombohedral phase decreases from $\Delta E_{FE} = 24$ to 2 meV for $x_{Mn} = 0$ to 0.5, respectively, indicating a weakening of the ferroelectricity with increasing Mn content. In Fig. 6(b) this energy gain is compared with the FE transition temperatures. Evidently, both parameters are strictly correlated, demonstrating that the FE Curie temperatures directly scale with ΔE_{FE}. The average local shifts of the Mn and Ge atoms obtained by DFT are presented in Fig. 6(c) versus Mn content, showing an overall linear decrease of the displacements with increasing Mn content and a factor of two smaller displacement for the Mn compared to the Ge atoms. Although the shift of the atoms in the calculations is not restricted to [111], it is found after lattice relaxation to be predominantly in this direction. Further both Mn and Ge atoms shift in the very same direction, which leads to a stronger change of the bond angles but allows us to maintain a more homogeneous distribution of bond lengths, rendering this configuration energetically more favorable. We also find that the displacements of Ge atoms adjacent to Mn atoms is significantly reduced compared to Ge atoms further away from Mn sites. These local variations are visualized as shaded areas in Fig. 6(c) and sketched schematically in Fig. 6(d). This effect nicely explains the overall decrease of the lattice distortions with increasing Mn content.

IV. DISCUSSION

Experiment and theory consistently show that the rhombohedral distortion angle decreases with increasing Mn content and is still nonzero at $x_{Mn} = 0.5$ at low temperature. This proofs that FE properties exist in the full solubility range and confirms that the unit cell angle alone cannot be used as a ubiquitous indicator for the FE transition. In fact, extrapolation of the theoretical and experimental data shown in Fig. 6(c) suggests that FE could extend even to $x_{Mn} > 0.6$ provided that the solubility could be maintained. It is also noted that at $x_{Mn} > 0.3$ we do not observe a sharp onset of a rhombohedral distortion in the epilayers. We attributed this to the fact that for $x_{Mn} > 0.3$ the epitaxial strain, caused by the lattice- and thermal expansion coefficient mismatch to the substrate, induces a rhombohedral distortion comparable to that of the FE phase transition. Thus, the onset of the FE phase transition is masked and can no longer be unambiguously detected.

Most importantly, experiments and calculations both reveal a very different displacement of Ge and Mn atoms in the ferroelectric phase transition. This is obviously a consequence of the different electronic structures of the two cations. For Mn, the electrons of the half-filled Mn $3d$ shell contribute to the chemical bonding. In particular, the wave function overlap with Mn $d_{3z^2-r^2}$ states and Mn $d_{x^2-y^2}$ states makes the bonds in the $\langle 100 \rangle$ directions more rigid [47], and leads to the tendency of Mn atoms positioning in the center of the surrounding Te atoms. In the Ge case this effect is absent, and moreover the two $4s$ electrons of Ge^{2+} ions do give rise to short-range repulsive forces resulting in a larger local lattice distortion. With increasing Mn content the atomic shifts of the Ge atoms decrease but remain nonzero even beyond the highest studied Mn concentration, and the same is found for the Mn atoms [cf. Fig. 6(c)]. While overall, these trends fit to the experimental data, for $x_{Mn} = 0.5$ the measured Mn and Ge shifts are slightly higher than the calculated values. We conjecture that this is due to the influence of epitaxial strain on the rhombohedral lattice distortions, which is significant only for high x_{Mn} where the intrinsic FE displacements are small and are thus more sensitive to external perturbations. In addition, the high vacancy concentrations [11] may also play a role in the lattice distortions, which will be addressed in further investigations. Here it must be noted that the thermal expansion coefficient mismatch is expected to strongly change with the Mn composition. While the thermal expansion of

GeTe [48] at room temperature is smaller than that of BaF_2 [49], existing bulk dilatation measurements of GeMnTe [50] show that with increasing Mn content the thermal expansion around room temperate is increasing reaching the one of BaF_2 around $x_{\mathrm{Mn}} = 0.2$. Looking in detail to the evolution of the unit cell angle in the paraelectric phase in Fig. S5 in Ref. [29] we indeed find a change of the slope around 20%. Accordingly with increasing Mn content the domain population is changing from the out of plane [111] direction to the tilted ⟨111⟩ directions. Therefore the thermal epitaxial strain is promoting the ferroelectricity in both cases.

The bond angles and distances display significant anomalies upon temperature changes and chemical doping [51]. According to our calculations the FE displacements of the Mn atoms in the host lattice cause local bond angle changes as large as four degrees (e.g., for $x_{\mathrm{Mn}} = 0.18$). In the context of a superexchange mediated ferromagnetism, this suffices to cross magnetic phase boundaries [52,53]. Since in our GeMnTe samples the free carrier (i.e., hole) concentration, which is assumed to be responsible for the ferromagnetic interactions, does not change significantly between $x_{\mathrm{Mn}} = 0.1$ to $x_{\mathrm{Mn}} = 0.48$, further contributions to the magnetic interactions are expected. Indeed a strong influence of the magnetic properties on the local atomic configurations in GeMnTe was found by DFT calculations as reported by Łusakowski *et al.* [12]. The high Mn composition also leads to frequent occurrence of Mn-Te-Mn bond configurations whose magnetic interaction cannot only be described by free carrier mediation but likely has contributions from exchange interactions which depend on the bond angles. The phase diagram depicted in Fig. 3 also shows that in the region with strong ferroelectricity, i.e., large deviations of the local bond angles from 90 degrees, the ferromagnetic order is suppressed. On the other hand, the ferromagnetic phase seems to be favored by the decrease of the atomic shifts of Mn and Ge, as revealed both by the EXAFS data and the DFT calculations. However, these off-center shifts are responsible for the ferroelectric behavior, and a strong interplay between the two ferroic orders was observed by ferromagnetic resonance experiments, reported in Ref. [5].

V. CONCLUSIONS

In summary, experimental investigations and first principles calculations of the local atomic structure of multiferroic $Ge_{1-x}Mn_xTe$ alloys reveal striking differences in the local displacements of Ge and Mn atoms. This is explained by the different electronic configurations of Ge and Mn, which makes the Mn bonds more rigid in the ⟨111⟩ directions, resulting in a smaller energy gain of the distorted FE phase. This explains both the overall decrease of the FE distortion as well as of the FE transition temperature with increasing Mn content. Together with results of magnetic investigations, the multiferroic phase diagram was derived, providing a guideline of the regimes where both FE and FM orders coexist and multiferroic behavior prevails. In particular, we predict that multiferroicity can be sustained up to temperatures of at least ~150 K for Mn concentrations between 30 and 40%, where the best compromise between FM interactions and FE distortions is obtained. Since $Ge_{1-x}Mn_xTe$ alloys feature the simplest atomic structure of multiferroic materials in which ferromagnetic and ferroelectric order originate from the same atomic site (Ge, Mn), these solid solutions provide a highly interesting model system for studies of multiferroic interactions and coupling.

ACKNOWLEDGMENTS

We thank G. Castro and S. Mangold at beamlines BM25/European Synchrotron Radiation source and XAS at ANKA for their support. This work was supported by the Czech Science Foundation (project No. 14-08124S) and the Austrian Science Fund (FWF): J3523-N27, SFB025-IRON.

APPENDIX: CALCULATION OF SUBLATTICE DISPLACEMENTS FROM X-RAY DIFFRACTED INTENSITIES

In Fig. 2(c) we show that the ratio of the intensities of the (333) and (222) Bragg diffractions, in the following named I_3 and I_2, respectively, varies when crossing the ferroelectric transition. We compare the intensity ratio with kinematical theory calculations.

Since our thin films absorb only weakly at the used x-ray photon energy of 20 keV the kinematical diffraction theory is perfectly suited to describe the diffracted intensities. Within this theory the intensities of Bragg peaks are proportional to the structure factor of the respective Bragg peak [54]. For (Ge,Mn)Te in the most general case the diffracted intensity for arbitrary (hkl) is given by:

$$I(h,k,l,a,\alpha,T,E) \propto \left| \sum_j o_j f_j(q,E) \mathrm{e}^{-W_j(T) q(h,k,l,a,\alpha)^2} \right.$$
$$\left. \times\, \mathrm{e}^{\imath q(h,k,l,a,\alpha)\cdot \vec{r}_j} \right|^2 . \tag{A1}$$

The sum runs over the atoms in one unit cell whose absolute positions in the unit cell are given by $\vec{r}_j$. $f_j(q,E)$ is the energy and momentum transfer q dependent atomic scattering factor, and via o_j, the occupation number of a specific lattice site, i.e., the chemical composition is included. In addition to the Miller indices this intensity depends on the unit cell parameters a and α, the x-ray photon energy E, and the temperature T. The temperature enters via the Debye Waller factor $\exp(-W_j(T)q^2)$ which we calculate using the Debye model [54]. For the Debye temperature of GeTe a value of 147 K is used, according to Ref. [55].

The relative coordinates of Ge and Mn within the unit cell are given by $(0-s,0-s,0-s)$, $(\frac{1}{2}-s,\frac{1}{2}-s,0-s)$, $(\frac{1}{2}-s,0-s,\frac{1}{2}-s)$, $(0-s,\frac{1}{2}-s,\frac{1}{2}-s)$, where s might take a distinct value for Mn and Ge. The Te sublattice positions are given by $(0+s,0+s,0+s)$, $(\frac{1}{2}+s,\frac{1}{2}+s,0+s)$, $(\frac{1}{2}+s,0+s,\frac{1}{2}+s)$, $(0+s,\frac{1}{2}+s,\frac{1}{2}+s)$. s_{Te} for Te is chosen to be equal to s_{Ge}. Considering symmetric Bragg reflections of $Ge_{1-x}Mn_xTe$ only, i. e., $(hkl) \equiv (hhh)$, Eq. (A1) can be simplified to

$$I_h(a,\alpha,T,E) \propto |4x F_{\mathrm{Mn}} \mathrm{e}^{-\imath 6\pi s_{\mathrm{Mn}} h} + 4(1-x) F_{\mathrm{Ge}} \mathrm{e}^{-\imath 6\pi s_{\mathrm{Ge}} h}$$
$$+ 4 F_{\mathrm{Te}} \mathrm{e}^{\imath 6\pi s_{\mathrm{Ge}} h}|^2, \tag{A2}$$

where $F_j = f_j \exp(-W_j(T)q^2)$ was used. We note that since we aim to describe the Bragg peak intensity of (222) and (333) peak only that our data are not sensitive to the type of transition, which can be either displacive or of order/disorder type [32]. In Eq. (A2) the dependence of the diffracted intensity on the unit cell parameters enters only in the q dependence of the atomic scattering factors and in the Debye-Waller factor and therefore is rather weak. In the high temperature cubic case, where $s_{\mathrm{Ge,Mn}} = 0.25$, the intensity is therefore high for even h ($I \propto |xF_{\mathrm{Mn}} + (1-x)F_{\mathrm{Ge}} + F_{\mathrm{Te}}|^2$) and low for odd h [$I \propto |xF_{\mathrm{Mn}} + (1-x)F_{\mathrm{Ge}} - F_{\mathrm{Te}}|^2$]. In Eqs. (A1) and (A2) we ignored constant prefactors, but we note that due to the polarized synchrotron radiation the polarization factor is unity and therefore does not need to be considered. For comparison with experimental data the change of the illuminated area at different Bragg peaks, however, has to be considered and we use the experimentally obtained lattice parameters and unit cell angles as shown in Fig. S5 in Ref. [29].

[1] J. Wang, J. B. Neaton, H. Zheng, V. Nagarajan, S. B. Ogale, B. Liu, D. Viehland, V. Vaithyanathan, D. G. Schlom, U. V. Waghmare, N. A. Spaldin, K. M. Rabe, M. Wuttig, and R. Ramesh, Science **299**, 1719 (2003).

[2] Y. Tokura, S. Seki, and N. Nagaosa, Rep. Prog. Phys. **77**, 076501 (2014).

[3] J. F. Scott, Nat. Mater. **6**, 256 (2007).

[4] Y.-H. Chu, L. W. Martin, M. B. Holcomb, M. Gajek, S.-J. Han, Q. He, N. Balke, C.-H. Yang, D. Lee, W. Hu, Q. Zhan, P.-L. Yang, A. Fraile-Rodríguez, A. Scholl, S. X. Wang, and R. Ramesh, Nat. Mater. **7**, 478 (2008).

[5] H. Przybylińska, G. Springholz, R. T. Lechner, M. Hassan, M. Wegscheider, W. Jantsch, and G. Bauer, Phys. Rev. Lett. **112**, 047202 (2014).

[6] R. W. Cochrane, M. Plischke, and J. O. Ström-Olsen, Phys. Rev. B **9**, 3013 (1974).

[7] Y. Fukuma, H. Asada, N. Nishimura, and T. Koyanagi, J. Appl. Phys. **93**, 4034 (2003).

[8] R. T. Lechner, G. Springholz, M. Hassan, H. Groiss, R. Kirchschlager, J. Stangl, N. Hrauda, and G. Bauer, Appl. Phys. Lett. **97**, 023101 (2010).

[9] M. Hassan, G. Springholz, R. T. Lechner, H. Groiss, R. Kirchschlager, and G. Bauer, J. Cryst. Growth **323**, 363 (2011).

[10] T. Dietl and H. Ohno, Rev. Mod. Phys. **86**, 187 (2014).

[11] T. Fukushima, H. Shinya, H. Fujii, K. Sato, H. Katayama-Yoshida, and P. H. Dederichs, J. Phys.: Condens. Matter **27**, 015501 (2015).

[12] A. Łusakowski, P. Bogusławski, and T. Story, J. Phys.: Condens. Matter **27**, 226002 (2015).

[13] W. Knoff, A. Łusakowski, J. Z. Domagała, R. Minikayev, B. Taliashvili, E. Łusakowska, A. Pieniążek, A. Szczerbakow, and T. Story, J. Appl. Phys. **118**, 113905 (2015).

[14] M. Kriener, T. Nakajima, Y. Kaneko, A. Kikkawa, X. Z. Yu, N. Endo, K. Kato, M. Takata, T. Arima, Y. Tokura, and Y. Taguchi, Sci. Rep. **6**, 25748 (2016).

[15] A. I. Lebedev, I. A. Sluchinskaya, V. N. Demin, and I. H. Munro, Phase Transitions **60**, 67 (1997).

[16] P. Dziawa, W. Knoff, V. Domukhovski, J. Domagala, R. Jakiela, E. Lusakowska, V. Osinniy, K. Swiatek, B. Taliashvili, and T. Story, *Narrow Gap Semiconductors 2007*, Springer Proceedings in Physics Vol. 119 (Springer, Netherlands, 2008), pp. 11–14.

[17] T. Chattopadhyay, J. X. Boucherle, and H. G. von Schnering, J. Phys. C: Solid State Phys. **20**, 1431 (1987).

[18] D. Lencer, M. Salinga, B. Grabowski, T. Hickel, J. Neugebauer, and M. Wuttig, Nat. Mater. **7**, 972 (2008).

[19] Edited by O. Madelung, U. Rössler, and M. Schulz, *Non-Tetrahedrally Bonded Elements and Binary Compounds I*, Landolt-Börnstein - Group III Condensed Matter, Vol. 41C (Springer-Verlag, Berlin, Heidelberg, 1998).

[20] A. V. Kolobov, D. J. Kim, A. Giussani, P. Fons, J. Tominaga, R. Calarco, and A. Gruverman, APL Mater. **2**, 066101 (2014).

[21] D. Yang, T. Chatterji, J. A. Schiemer, and M. A. Carpenter, Phys. Rev. B **93**, 144109 (2016).

[22] S. Picozzi, Front. Phys. **2**, 10 (2014).

[23] M. Liebmann, C. Rinaldi, D. Di Sante, J. Kellner, C. Pauly, R. N. Wang, J. E. Boschker, A. Giussani, S. Bertoli, M. Cantoni, L. Baldrati, M. Asa, I. Vobornik, G. Panaccione, D. Marchenko, J. Sánchez-Barriga, O. Rader, R. Calarco, S. Picozzi, R. Bertacco, and M. Morgenstern, Adv. Mater. **28**, 560 (2016).

[24] J. Krempaský, H. Volfová, S. Muff, N. Pilet, G. Landolt, M. Radović, M. Shi, D. Kriegner, V. Holý, J. Braun, H. Ebert, F. Bisti, V. A. Rogalev, V. N. Strocov, G. Springholz, J. Minár, and J. H. Dil, arXiv:1503.05004.

[25] J. J. Gervacio-Arciniega, E. Prokhorov, F. J. Espinoza-Beltrán, and G. Trapaga, J. Appl. Phys. **112**, 052018 (2012).

[26] J. E. E. Baglin and J. S. Wiliams, in *Ion Beams for Materials Analysis*, edited by R. Curtis Bird and J. S. Williams, Vol. 103-148 (Academic Press, Sydney, 1989).

[27] J. F. van der Veen, Surf. Sci. Rep. **5**, 199 (1985).

[28] M. Mayer, SIMNRA, a simulation program for the analysis of NRA, RBS and ERDA, in *Proceedings of the 15th International Conference on the Application of Accelerators in Research and Industry*, edited by J. L. Duggan and I. L. Morgan, AIP Conf. Proc. Vol. 475 (AIP, Melville, NY, 1999), p. 541.

[29] See Supplemental Material at http://link.aps.org/supplemental/10.1103/PhysRevB.94.054112 for additional experimental data.

[30] Edited by O. Madelung, U. Rössler, and M. Schulz, *Non-Tetrahedrally Bonded Binary Compounds II*, Landolt-Börnstein - Group III Condensed Matter, Vol. 41D (Springer-Verlag, Berlin, Heidelberg, 2000).

[31] All Miller indices refer to the cubic or derived rhombohedral unit cell description instead of the smaller primitive rhombohedral cell, respectively.

[32] P. Fons, A. V. Kolobov, M. Krbal, J. Tominaga, K. S. Andrikopoulos, S. N. Yannopoulos, G. A. Voyiatzis, and T. Uruga, Phys. Rev. B **82**, 155209 (2010).

[33] J. M. Hudspeth, T. Chatterji, S. J. L. Billinge, and S. A. J. Kimber, arXiv:1506.08944.

[34] B. Ravel and M. Newville, J. Synchro. Rad. **12**, 537 (2005).

[35] S. D. Kelly, E. A. Stern, and R. Ingalls, J. Synchro. Rad. **8**, 311 (2001).

[36] J. C. Mikkelsen, Jr. and J. B. Boyce, Phys. Rev. B **28**, 7130 (1983).
[37] A. Balzarotti, N. Motta, A. Kisiel, M. Zimnal-Starnawska, M. T. Czyznyk, and M. Podgórny, Phys. Rev. B **31**, 7526 (1985).
[38] I. Grinberg, V. R. Cooper, and A. M. Rappe, Nature (London) **419**, 909 (2002).
[39] A. Al-Zein, G. Fraysse, J. Rouquette, P. Papet, J. Haines, B. Hehlen, C. Levelut, G. Aquilanti, and Y. Joly, Phys. Rev. B **81**, 174110 (2010).
[40] G. Kresse and J. Furthmüller, Comput. Mater. Sci. **6**, 15 (1996).
[41] G. Kresse and D. Joubert, Phys. Rev. B **59**, 1758 (1999).
[42] M. Dion, H. Rydberg, E. Schröder, D. C. Langreth, and B. I. Lundqvist, Phys. Rev. Lett. **92**, 246401 (2004).
[43] G. Román-Pérez and J. M. Soler, Phys. Rev. Lett. **103**, 096102 (2009).
[44] J. Klimeš, D. R. Bowler, and A. Michaelides, Phys. Rev. B **83**, 195131 (2011).
[45] V. I. Anisimov, J. Zaanen, and O. K. Andersen, Phys. Rev. B **44**, 943 (1991).
[46] S. L. Dudarev, G. A. Botton, S. Y. Savrasov, C. J. Humphreys, and A. P. Sutton, Phys. Rev. B **57**, 1505 (1998).
[47] M. Krause and F. Bechstedt, J. Supercond. Novel Magn. **26**, 1963 (2013).
[48] E. A. Marchenkov and V. P. Shipul', J. Eng. Phys. Therm. **66**, 547 (1994).
[49] N. Neumann, G. Kommichau, W. Schmitz, and B. Schumann, J. Mater. Sci. Lett. **5**, 1131 (1986).
[50] N. Abrikosov, E. Avilov, O. Karpinskii, and L. Shelimova, Izv. Akad. Nauk SSSR, Neorg. Mater. **16**, 255 (1980).
[51] J. K. Lee, M. W. Oh, B. S. Kim, B. K. Min, H. W. Lee, and S. D. Park, Electron. Mater. Lett. **10**, 813 (2014).
[52] N. Ray and U. V. Waghmare, Phys. Rev. B **77**, 134112 (2008).
[53] F. Jiménez-Villacorta, J. A. Gallastegui, I. Fina, X. Marti, and J. Fontcuberta, Phys. Rev. B **86**, 024420 (2012).
[54] U. Pietsch, V. Holý, and T. Baumbach, *High-Resolution X-Ray Scattering* (Springer-Verlag, New York, 2004).
[55] Y. Ishihara, Y. Yoshita, and I. Nakada, J. Phys. Soc. Jpn. **55**, 1948 (1986).